Photoelectrochemical and theoretical investigation of the photocatalytic activity of TiO2:N

4 authors:

Gabriela Byzynski Soares
São Paulo State University
33 PUBLICATIONS 163 CITATIONS
SEE PROFILE

Renan A. P. Ribeiro
Universidade Federal de São Carlos
28 PUBLICATIONS 86 CITATIONS
SEE PROFILE

Sergio R. de Lazaro
State University of Ponta Grossa
74 PUBLICATIONS 771 CITATIONS
SEE PROFILE

Caue Ribeiro
Brazilian Agricultural Research Corporation (EMBRAPA)
209 PUBLICATIONS 3,670 CITATIONS
SEE PROFILE

Some of the authors of this publication are also working on these related projects:

Energy View project

Multiferroic and magnetic materials View project

Photoelectrochemical and theoretical investigation of the photocatalytic activity of TiO$_2$: N

Gabriela Byzynski Soares,*[ab] Renan Augusto Pontes Ribeiro,[c] Sergio Ricardo de Lazaro[c] and Caue Ribeiro[b]

Electrochemical and photoelectrochemical techniques have been employed to investigate the electronic energy level modification of N-doped TiO$_2$ and to elucidate its properties and roles, particularly the electron transfer rate and influence on recombination, in a simple and facile manner. However, the results obtained cannot be easily interpreted and they need comparisons with theoretical calculations. In this study, photoelectrochemical measurements were conducted to investigate the effect of N-doping on TiO$_2$ nanomaterials, and the results obtained were compared with theoretical calculations. Band-gap values calculated by diffuse reflectance UV-vis spectroscopy were used together with photoelectrochemical measurements of TiO$_2$ and TiO$_2$: N flat-band potentials to create a scheme of the energy-level band edges. In addition, this method confirmed the creation of energetic inter-levels by the N-doping process, as predicted by theoretical calculations. The replacement of an oxygen atom by nitrogen atom in the anatase structure shows a modification of the energetic levels, caused by a shift of the upper energy level; this shift was caused by local structural disorder. From the photoelectrochemical results, it is possible to confirm that the electron concentration in the TiO$_2$ photoelectrode is higher than that in the TiO$_2$: N photoelectrode; due to an increase in the recombination of electrons and holes because of the creation of inter-levels in the TiO$_2$: N band-gap. In addition, theoretical analysis indicated a possibility of direct transfer of electrons into the band-gap of TiO$_2$: N. This combined approach was useful for interpreting many unclear results with respect to the photocatalytic activity of TiO$_2$: N.

1   Introduction

In semiconductor materials, photoexcitation is a beneficial process in oxidative reactions because of generation of electron–hole pairs, which migrate to the surface and catalyze these reactions.[1–7] Materials such as ZnO, ZnS, and TiO$_2$ exhibit these desirable characteristics conductive for photocatalysis due to large band-gaps ranging from 2.0 eV to 3.5 eV.[8–11] However, the photocatalytic behavior associated with these materials is limited to the high-energy ultraviolet (UV) region of the sunlight spectrum. Meanwhile, one method for modifying the electronic properties of these materials is to dope them with metals and/or nonmetals during semiconductor synthesis.[12–19] This strategy has been reported to improve the energy absorption range by reducing the band-gap or creating donor–acceptor levels in the

band-gap. Although it is reasonable to hypothesize the generation of extra energy levels between the conduction (CB) and valence (VB) bands in TiO$_2$-doped nanoparticles (energetic inter-levels), it is not well understood if these levels can increase electronic recombination, and consequently, effectively alter photocatalytic activity.

The TiO$_2$: N doping process is categorized as anion doping, which is different from the typical cation doping process.[20,21] Anion doping alters the negative charge balance in the semiconductor by forming interstitial inclusions or substitutional dopants (where O^{2-} in the network is replaced by N^{3-}). Although defects and dopants in TiO$_2$ are typically paramagnetic, electron paramagnetic resonance (EPR) spectroscopy is one of the methods employed to identify their effect.[22] X-ray photoelectron spectroscopy (XPS) is also useful for identifying interstitial or substitutional N-doping in TiO$_2$.[23] However, both these methods are expensive and may be not adequate for analysis. Therefore, it is imperative to develop alternative techniques to characterize these catalysts.

In this regard, electrochemical and photoelectrochemical techniques have been applied to evaluate the actual N-doping effect, which generates new energy levels between the CB and VB in the band-gap of TiO$_2$. These techniques exhibit

[a]Paulista State University "Julio de Mesquita Filho", UNESP, Campus Araraquara. Prof. Francisco Degni Street, 55, Quitandinha, 14800-060, Araraquara, SP, Brazil. E-mail: gabi.byzynski@gmail.com

[b]Embrapa Instrumentation, XV de Novembro Street, 1452, 13560-970, São Carlos, SP, Brazil

[c]Ponta Grossa State University (UEPG), Applied Chemistry Postgraduate Program, Chemistry Department, Av. Gen. Carlos Cavalcanti, 4748, Uvaranas, 84030-000, Ponta Grossa, PR, Brazil

advantages of possible direct evaluation of the transfer of electrons during the photocatalytic process as well as the characterization of important features such as the quasi-Fermi level of doped oxides.[24] Mott–Schottky plots are representative of these techniques and are determined by impedance spectroscopy. With these plots, it is possible to determine the so-called flat-band potential (V_{fb}) of a bulk semiconductor electrode.[24]

When the interface between a semiconductor and an electrolyte is illuminated with energy higher than its band-gap energy, electron–hole pairs are generated at the electrode surface. The junction of the semiconductor/electrolyte interface, caused when the semiconductor is in contact with an electrolyte, determines the electron hole separation kinetics. To reach the equilibrium condition, the junction in a redox electrolyte causes a change in the electrochemical potential, which allows the flow of charge from one phase to another. Generally, this shift of electrochemical potential promotes bending in the energy edges (conduction and valence band) and the region where there is bending is called the space charge layer. The space charge layer is characterized by the accumulation of electrons or holes at the surface, depending the semiconductor type (n or p-type) and the redox potential of the electrolyte. When the potential across the space charge region approaches zero, the resultant charge transferred is zero. This potential is known as the flat-band potential and is an important parameter for bulk semiconductor photoelectrodes.[24] Other examples are the relation between the incident photon-to-current efficiency (IPCE) and the absorption wavelength[25] and the Mott–Schottky plots, which are typically used for the characterization of dye- and quantum-dot-sensitized solar cells. However, it is essential to interpret the results obtained by photoelectrochemical measurements, and it is desirable to compare these results with those from theoretical calculations as *ab initio* methods can aid in the understanding of the possible processes during charge photogeneration.

Thus, this study investigates the modification of N-doped TiO$_2$'s electronic energy levels and elucidates its properties and roles, particularly the electron transfer rate and influence on charge recombination, in a simple and facile manner. For this purpose, photoelectrochemical measurements were conducted in a manner similar to measurements conducted for dye- and quantum-dot-sensitized solar cells. Cyclic voltammetry was employed to determine the quasi-Fermi level potential of TiO$_2$ and TiO$_2$: N embedded in carbon paste solid electrodes, and diffuse reflectance spectroscopy (DRS) was employed together with V_{fb} results to obtain a simplified scheme of the energy edges. An electrochemical model was applied to determine the concentration of electrons in each electrode as well as the electron transfer rate. To understand the photoelectrochemical results, theoretical calculations of the density of states (DOS) and effective band-gaps were performed for a comparative analysis. This work is not intended for a direct comparison between the absolute results derived from theoretical calculations and those obtained from characterization measurements but for a tentative evaluation between the results and the relative Fermi levels with the nitrogen content variation.

This combined approach is a useful, fast, and easy tool for understanding the influence of the generation of energy levels on the photocatalytic behavior of these doped materials. In addition, this approach can also be applied to future research on other anion-doped TiO$_2$ materials.

2 Materials and methods

2.1 TiO$_2$ nanoparticle synthesis

Titanium(IV) resins were prepared using a polymeric precursor method. First, titanium tetraisopropoxide (Merck) was dissolved in an aqueous citric acid solution (Merck) at 75 °C in a molar ratio of 1 : 3. After complete dissolution and homogenization using a magnetic stirring bar, the titanium citrate was polymerized by the addition of ethylene glycol (Merck). Nitrogen-doped resins were prepared by the same route, except for the addition of 2% urea (weight equivalent TiO$_2$) before heat treatment, which was carried out for all samples, as previously reported by Soares *et al.*[15] Diffuse reflectance UV-Vis spectra were recorded on an ultraviolet-visible-near-infrared (UV-Vis-NIR) Cary 5G spectrophotometer. Prior to each measurement, the substrate spectrum was taken as the baseline. UV-Vis spectra were obtained in diffuse-reflectance mode (R) and transformed to a magnitude proportional to the extinction coefficient (K) by the Kubelka–Munk model, which relates the extinction coefficient and scattering (S) with the reflectance ($K/S = (1 - R)^2/2R$). For comparison, all spectra were arbitrarily normalized at an intensity of 1.0. The band-gap values obtained for TiO$_2$ and TiO$_2$: N were 2.99 eV and 2.87 eV, respectively.[15]

2.2 Preparation and characterization of the composite electrodes

For electrochemical characterization, carbon paste electrodes were packed in 1 mL syringes. Different amounts of TiO$_2$ (15% and 60%) (w/w) were vigorously mixed in a mortar with graphite powder (Dinamica), and the resultant powder was suspended in mineral oil (3.0 mg : 0.3 mL of graphite powder : mineral oil). Voltammetric experiments were performed using a potentiostat–galvanostat (Autolab PGSTAT 30). The carbon paste electrodes were characterized by cyclic voltammetry (CV) using a K$_3$Fe(CN)$_6$ solution (Merck) (0.05 mol L^{-1}) as the electrolyte and three electrodes: a saturated calomel electrode (SCE), platinum wire, and TiO$_2$ carbon paste as the reference, counter, and working photoelectrodes, respectively. The set up used to conduct the voltammetric measurements was similar to that proposed by our previously work.[26]

2.3 Computational details

The structural and electronic properties of both pure and doped TiO$_2$ anatase were investigated by first principles calculations based on Density Functional Theory (DFT) using the B3LYP hybrid functional[27,28] augmented with a Long-Range Dispersion correction (B3LYP+D)[29] and all calculations were performed using the CRYSTAL09 package.[30] First of all, the experimental unit cell for pure TiO$_2$ was fully-relaxed (cell parameters and atomic positions) as a function of the total energy of the system.

Substitutional paramagnetic (N^2) and diamagnetic (N^{3-}) doping on bulk anatase was modelled by replacing one and two oxygen atoms in a $2 \times 2 \times 1$ supercell (48 atoms), respectively. Furthermore, the diamagnetic scenario requires the creation of oxygen vacancies, which was modelled by removing one oxygen atom of the supercell, as presented in Fig. 1b. Otherwise, in order to take the surface effects on the nitrogen doping process into account, a (001) periodic slab was cleaved from the optimized anatase unit cell consisting of a slab thickness of 18-layers, where one outermost oxygen (2c) atom was replaced by N^2 (Fig. 1c). Theoretical reports suggest that both anionic and cationic doping processes located on the surface layer are more favorable than those at subsurface ones.[31,32] It is important to clarify that only substitutional nitrogen species were considered due to the similarity between the electronic structures obtained with substitutional/interstitial species, as reported by other theoretical studies.[33–35] The optimization process was controlled by mono- and bielectronic integrals converged with pre-defined criteria in 10^{-8} Hartree. Thresholds for convergence on the RMS gradient, RMS displacement, maximum gradient and maximum displacement were set to 3×10^{-5}, 1.2×10^{-4}, 4.5×10^{-5} and 1.8×10^{-5} a.u., respectively. Diagonalization of the matrix density was carried out using a grid of k points in reciprocal space according to the Monkhorst–Pack method[36] and the shrink factor was set to 8×8 (Gilat Web) corresponding to 59, 170 and 34 independent points, k, in the Brillouin zone for the pure, supercell N-doped and slab N-doped TiO$_2$, respectively. The level of accuracy in evaluating the Coulomb and exchange series was controlled by five thresholds, for which values 10^{-7}, 10^{-7}, 10^{-7}, 10^{-7} and 10^{-14}, are suggested for magnetic materials.[37] The Ti, O and N atoms were described by the all-electron atom-centered Gaussian-type basis sets 8-6411(31d)G, 8-411(1d)G and 6-31d1G, respectively.[38,39]

3 Results and discussion

3.1 Electroanalytical characterization

The electron transfer ability of the obtained photoelectrodes was evaluated in the presence of the Fe(CN)$_6^{(3-/4-)}$ redox system, which is globally employed as a standard system to obtain information about heterogeneous electron transfer rates.[26,40] Fig. 2 shows the current–potential characteristics for the carbon paste electrode with and without TiO$_2$ (15% w/w) and TiO$_2$: N (15% w/w), in the dark and under UVC radiation at 20 mV s^{-1} in N-purged 0.05 M K$_3$Fe(CN)$_6$, pH 7.0. The thickness of the electrodes was 50 mm, and the geometric area of the electrode surface was 7.1 mm^2.

As shown in Fig. 2a, the carbon paste photoelectrode without TiO$_2$ also presented an electrochemical response for the Fe(CN)$_6^{(3-/4-)}$ redox system, and the photoelectrode containing TiO$_2$ (Fig. 2b) exhibited an anodic current density lower than that of the electrode without TiO$_2$. Electron transfer kinetics are significantly influenced by the electrode surface arrangement and some defects or deformation in the photoelectrode surface could modify the electron transfer process.[40] Considering a semiconductor material (TiO$_2$) dispersed in a conductive matrix (carbon paste electrode) will present surface polarization under an external electrical field, the resulting material may have some deviations due to OH$^-$ charges on TiO$_2$, related to the number of interfaces (TiO$_2$/carbon contact). The presence of TiO$_2$ in the carbon paste matrix diminished the contact points for conduction, decreasing the resultant peak current with respect to the carbon paste electrode.[26]

Under UVC illumination, the maximum photocurrent increased in both cases for the TiO$_2$-free carbon paste (Fig. 2a) and TiO$_2$/carbon paste photoelectrodes (Fig. 2b). The TiO$_2$-free carbon paste electrode (Fig. 2a) exhibits a photocurrent under UVC illumination probably caused by the photoelectric effect.[26] However, this increase was clearly more significant for the TiO$_2$-containing electrode (Fig. 2b), indicating a positive synergistic effect on the specific capacitance of the electrode. The presence of TiO$_2$ in the matrix electrode clearly modifies the electron transfer mechanism on the electrode surface and this process could be interfered with by electronic transfer kinetics and electronic diffusion in the electrolyte solution, considering a mixed-control regime.[41] Under illumination, the TiO$_2$/carbon paste electrode provides better electronic conductivity compared to that without illumination.

Fig. 2c presents the behavior of the TiO$_2$: N/carbon paste photoelectrode and, in this case, should highlight the alteration
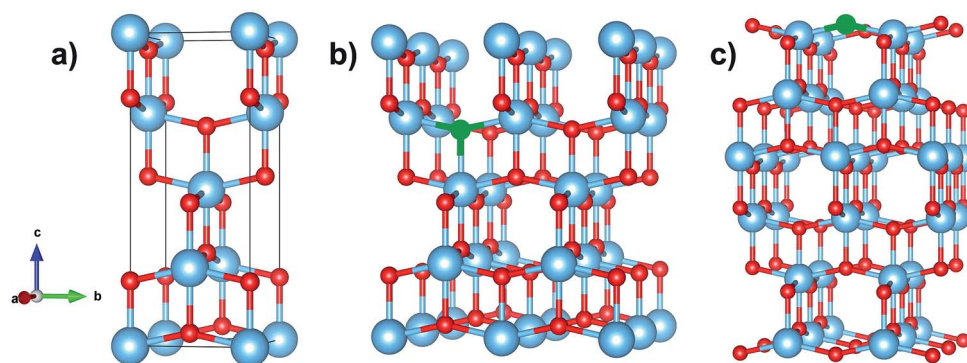

Fig. 1 Periodic models for pure and doped anatase TiO$_2$. (a) Crystallographic unit cell. (b) $2 \times 2 \times 1$ supercell doped with nitrogen at a three-fold coordinated anionic site. (c) 001-surface oriented 18-layer periodic slab, 18-layers doped with nitrogen at the two-coordinated outermost oxygens. Blue, red and green balls represent the titanium, oxygen and nitrogen atoms, respectively.
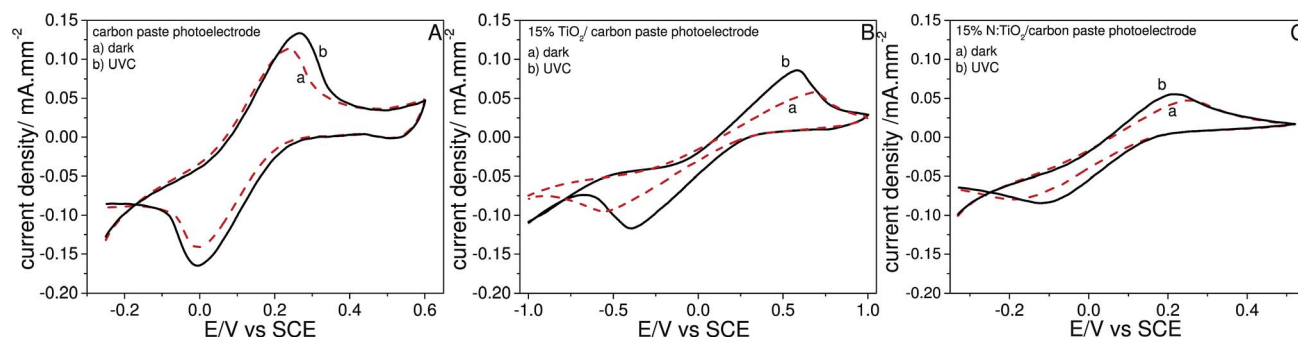
Fig. 2 CVs of different carbon paste electrodes in the dark and with UVC illumination (a) 15% TiO_2/carbon paste electrode and carbon paste electrode, (b) 15% N (2%) : TiO_2/carbon paste electrode and 15% TiO_2/carbon paste electrode. Scan rate = 20 mV s^{-1}; electrolyte solution: (K$_3$Fe(CN)$_6$), 0.05 mol L^{-1}, under N-purged atmosphere, at ambient temperature.

in the photoelectrode characteristics only by the embedded different material's characteristics as a doped semiconductor, confirming the difference between pristine TiO_2 and N doped TiO_2. This difference is promoted especially by defects in the TiO_2 lattice induced during the doping process, as oxygen vacancies, which influence in the final conductivity.

It is evident that the presence of TiO_2 in the carbon paste electrode modifies the conduction properties of carbon paste, as confirmed by the voltammetric data shown in Fig. 2. The peak-to-peak separation (ΔE) between the reduction and oxidation signals in Fig. 2 can provide the heterogeneous electron transfer rate constant (ψ) by the Nicholson method and then, the rate of electron transfer can be obtained (k_0).[40] From Fig. 2, it is possible to observe that the TiO_2/carbon paste photoelectrode shows the largest ΔE (978 mV vs. SCE), followed by the SCE : N/carbon paste photoelectrode (329 mV vs. SCE). The carbon paste electrode displays the smallest ΔE (278 mV vs. SCE). The diffusion coefficients used for the calculations were $D_O = D_R = 7.26 \times 10^{-6}$ cm^2 s^{-1}.[42] Comparing the three electrodes, the carbon paste electrode offered the fastest electron transfer ($k_0 = 3.39 \times 10^{-4}$ cm s^{-1}), as expected. In the presence of TiO_2 nanoparticles, the rate constant of electron transfer is reduced to 6.46×10^{-5} cm s^{-1} and for TiO_2 : N, k_0 shows a slightly decrease compared with the carbon paste electrode (2.66×10^{-4} cm s^{-1}), indicating the N-doping influence on electron transfer in the photoelectrodes.

Some important defining aspects of semiconductor electrochemistry should be highlighted, such as the Fermi level which is defined as the occupation description of energy levels in a semiconductor at thermodynamic equilibrium. However, the thermodynamic equilibrium situation is not always satisfied, especially when electrons and holes are in excess under semiconductor illumination or injected under electric bias. For this reason, the electron and hole densities in the conduction and valence bands are defined by a quasi-Fermi level of electrons and quasi-Fermi level of holes. When a photon reaches the semiconductor's surface, creating a charge pair electron–hole, the density of majority carriers (electrons, in the case of TiO_2) does not expressly increase upon illumination and the quasi-Fermi level of electrons is almost the same compared with the Fermi level at thermodynamic equilibrium. On the other hand,

the density of minority carriers (holes) increases by many orders of magnitude, and this leads to a shift of the quasi-Fermi level of holes. Only for heavily doped n-type metal oxides like TiO_2, is the lower conduction band edge (E_{CB}) practically unified with the quasi-Fermi level of electrons.

Now, consider the introduction of an electrode in a photoelectrochemical system, with an electrode surface in contact with an electrolyte solution. After contact of the semiconductor surface (electrode) with the electrolyte, thermodynamic equilibrium is established on both sides by adjustment of the Fermi level of the semiconductor with the Fermi level of the electrolyte ($E_{F,redox}$). As $E_{F,redox}$ is considered constant, to reach the equilibrium, electron transfer should occur across the interface, resulting in space charge layer formation (a depletion layer). In the case of an n-type semiconductor, electron transfer creates an excess of positive charges on the semiconductor surface. Consequently, negative charges are located in the electrolyte solution. In this situation, the electric field of the negative charges on the electrolyte obstructs electron transfer until thermodynamic equilibrium is reached. As a result, no net charge flow happens and this condition is known as the flat band potential (V_{fb}).[24,43] So, in a thermodynamic equilibrium between the electrode surface and electrolyte, V_{fb} has the same energy value as the quasi-Fermi level of electrons in TiO_2, or the same value as E_{CB}.

As a consequence, the conduction and valence bands are bent upwards. However, the bent bands only apply to thin compact highly doped TiO_2 films. In the context of nanomaterials, as presented in this case for TiO_2 nanoparticles (crystallite size = 10 nm) and TiO_2 : N (crystallite size = 7 nm), and in an exceedingly porous nanocrystalline electrode such as carbon paste electrodes, the space-charge layer formation does not occur due to the small crystallite size of the semiconductor.[43] In this case, the small TiO_2 crystal does not contain enough electrons in order to create an effective space-charge layer.

With the support of the Buttler equation[20] is possible to determine the flat band potential of each semiconductor:

$$j^2 = \left(\frac{2q\varepsilon\varepsilon_0 I_0^2 \alpha^2}{N_d} \right) (V - V_{fb}) \tag{1}$$

where j is the photocurrent density, q is the transferred charge per ion, ε is the permittivity of the surroundings, ε_0 is the vacuum permittivity, I_0 is the current density difference, α is the optic absorption coefficient, N_d is the number of charge donors, V is the potential, and V_{fb} is the flat band potential. The flat band potential may thus be regarded as the potential for the onset of the square photocurrent obtained in Fig. 3.[21,44] In this way, Fig. 3 is derived from Fig. 2, and shows the V_{fb} for the TiO$_2$ composite photoelectrode of 0.112 V $vs.$ SCE and for the TiO$_2$: N composite photoelectrode of 0.049 V $vs.$ SCE, in 0.05 M K$_3$Fe(CN)$_6$, pH 7.0. The values of V_{fb} are important to obtain direct information on the position of the CB edge in n-type semiconductor materials, since it could be assumed that the difference between V_{fb} and E_{CB} is insignificant. In this way, measurement of V_{fb} shows the conduction band edge determination of thin compact TiO$_2$ electrodes.[43] The obtained values of E_{CB} are -0.132 V $vs.$ NHE and -0.195 V $vs.$ NHE for the TiO$_2$ composite electrode and the TiO$_2$: N composite electrode, respectively. It is important to highlight that these values are presented for Fe(CN)$_6^{(3-/4-)}$ solution in pH = 7 and are also dependent on material characteristics which are related to the synthesis method.

Spadavecchia $et\ al.$[33] present an extensive comparison between the determination of V_{fb} by the Mott–Schottky plot and photovoltage/photocurrent method/spectroelectrochemistry of TiO$_2$ and TiO$_2$: N different electrodes. It is important to note that the V_{fb} variation is dependent on the electrolyte pH and material synthesis methods used, showing a large deviation in values. In this way, the results presented here are in accordance with those reported by Spadavecchia $et\ al.$[33] Typically, the V_{fb} value shifts in the negative direction for the TiO$_2$: N electrode.[45,46] For instance, as described by Xiang $et\ al.$,[45] for a mesoporous nitrogen-doped TiO$_2$ sphere used in quasi-solid-state dye-sensitized solar cells, the doped structure exhibits a shift of 0.13 V $vs.$ SCE for more negative values as compared to the undoped structure.

Fig. 4 shows the energy scheme with the E_{CB} and E_{VB} values relative to the hydrogen standard electrode potential, for the TiO$_2$ and TiO$_2$: N photoelectrodes shown in Fig. 2 and 3. The determination of the E_{CB} often explains the measurement of the
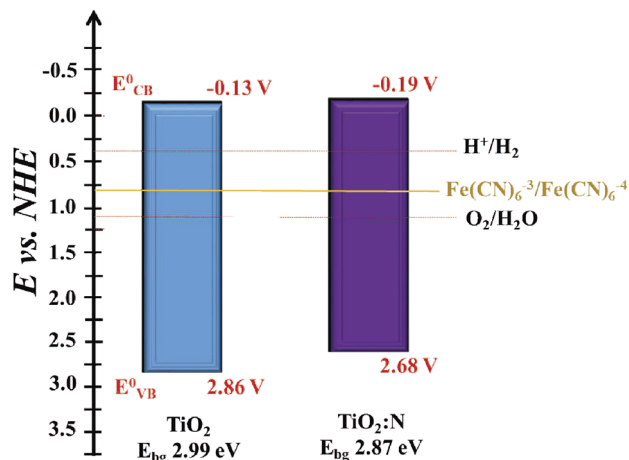
Fig. 4 Conduction and valence bands schematic of the photo-electrodes with semiconductors TiO$_2$ and TiO$_2$: N in pH = 7 (H$^+$/H$_2$ redox potential = 0.414 V (pH 7.0), O$_2$/H$_2$O redox potential = 1.109 V, Fe(CN)$_6^{3-}$/Fe(CN)$_6^{4-}$ redox potential = 0.770 V in pH 7.0). $This\ figure$ $takes\ the\ electrochemical\ convention\ energy\ scale\ into\ consideration.$

position of the quasi-Fermi level of electrons in the TiO$_2$ photoelectrodes. Once this is known, the E_{VB} values can be simply calculated by adding the value of band-gap energy that is presented in Section 2.1 of a paper by Soares $et\ al.$[15] to obtain V_{fb} for each of the photoelectrodes. Because N-doping causes a decrease in the band-gap values of the semiconductor, an electric field is necessary to maintain the separation of the photogenerated charges.[47]

As shown in Fig. 3, the E_{CB} values of the TiO$_2$ and TiO$_2$: N photoelectrodes were -0.132 V and -0.195 V $vs.$ NHE, respectively. The potential values shifted to more negative values after doping, and together with the results shown in Fig. 4, these results indicate that N-doping actually creates new energy levels between the CB and VB, known as inter-levels, in the TiO$_2$ band-gap.[46] Some authors have termed these new energy levels between the CB and VB of TiO$_2$ as intralevels; however, this name is not representative of the location of the new energy levels.[13,17] The variation in V_{fb} after doping was in accordance with other dopants such as F and is due to the higher abundance of electrons in the doped nanoparticles.[48] Consequently, the deformation of the energy level caused by N doping decreased the effective energy amount required for excitation of an electron in the VB to the CB in the case of surface photoexcitation.[49] Beranek $et\ al.$ have observed similar behavior[25] by employing capacitive spectral-resolved surface photovoltage and IPCE measurements, affirming that recombination becomes more efficient as the band-gap reaches low values. However, the shift of V_{fb} induced by N doping is not only an effect of the presence of nitrogen on the TiO$_2$ lattice; it is well known that the visible activity of TiO$_2$: N is caused due to diverse factors such as the presence of oxygen vacancies caused by the doping methods, the electron–hole recombination rate and morphological/structural properties of the material. The presence of N in a TiO$_2$ lattice could be considered as being in an interstitial or substitutional way, in other words, in space
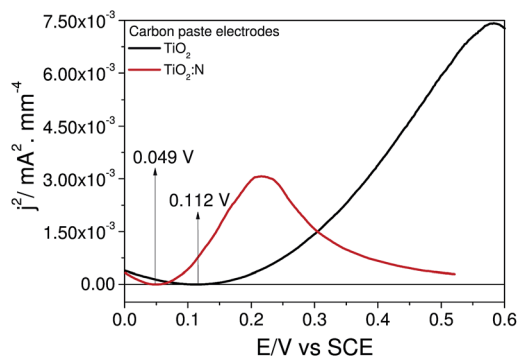

Fig. 3 Square of the anodic photo-current shown in Fig. 2 of the different carbon paste electrodes (TiO$_2$ and N (2%) : TiO$_2$) with UVC illumination.
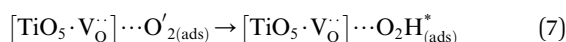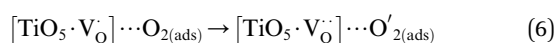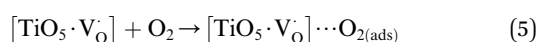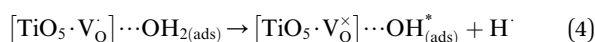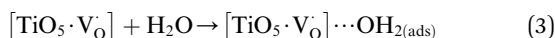
sites or in O sites in the TiO_2 lattice. In both ways, there is a charge compensation, causing O vacancies. It is possible to describe the TiO_2 photoexcitation based on the clusters model, in which $[TiO_6]^x$ is associated with neutral ($V_O^\times$), mono-ionized ($V_O^{\cdot}$) or di-ionized ($V_O^{\cdot\cdot}$) oxygen vacancies. First of all, the creation of a hole-pair is required as:

$$[TiO_6]^x + [TiO_5 \cdot V_O^\times] \rightarrow [TiO_6]' + [TiO_5 \cdot V_O^{\cdot}] \tag{2}$$

Subsequently, the hydroxyl radical (OH*) (eqn (3) and (4)) and superoxide radical (O_2H*) (eqn (5)–(7)) occur, with water and molecular oxygen adsorbed on the surface of the material, respectively.

$$[TiO_5 \cdot V_O^{\cdot}] + H_2O \rightarrow [TiO_5 \cdot V_O^{\cdot}] \cdots OH_{2(ads)} \tag{3}$$

$$[TiO_5 \cdot V_O^{\cdot}] \cdots OH_{2(ads)} \rightarrow [TiO_5 \cdot V_O^\times] \cdots OH_{(ads)}^* + H^{\cdot} \tag{4}$$

$$[TiO_5 \cdot V_O^{\cdot}] + O_2 \rightarrow [TiO_5 \cdot V_O^{\cdot}] \cdots O_{2(ads)} \tag{5}$$

$$[TiO_5 \cdot V_O^{\cdot}] \cdots O_{2(ads)} \rightarrow [TiO_5 \cdot V_O^{\cdot\cdot}] \cdots O'_{2(ads)} \tag{6}$$

$$[TiO_5 \cdot V_O^{\cdot\cdot}] \cdots O'_{2(ads)} \rightarrow [TiO_5 \cdot V_O^{\cdot\cdot}] \cdots O_2H_{(ads)}^* \tag{7}$$

In the case of the $TiO_2 : N$ material, there are more reactions involved in the mechanism. First, $[TiO_6]^x$ is associated with a neutral oxygen vacancy $[TiO_5 \cdot V_O^\times]$ in the presence of an N source (N_{source}).

$$[TiO_6]^x + [TiO_5 \cdot V_O^\times] + N_{source} \rightarrow [TiO_6N]' + [TiO_5 \cdot V_O^{\cdot}] \tag{8}$$
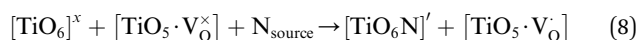
The resulting $[TiO_6N]'$ presents a negative charge characteristic and should stabilize the creation of more oxygen vacancies ($[TiO_5 \cdot V_O^{\cdot}], [TiO_5 \cdot V_O^{\cdot\cdot}]$) compared with the undoped TiO_2 material, promoting a modification in radical production and then in the surface material characteristics. The differences in the E_{CB} and E_{VB} values observed in Fig. 4 between the doped and undoped TiO_2 seem to be small, however it should be noted that a small shift in these values could produce a change in energy level of tens of millivolts, enabling some applications of TiO_2 : N that are not possible for the TiO_2 material.

One of the most important parameters related to the efficiency of charge recombination is electron lifetime, which can be calculated by intensity-modulated photovoltage spectroscopy; however, it is not useful for elements that exhibit a significant potential difference at the open circuit. To avoid this limitation, two parameters can be employed: open-circuit voltage decay (OCVD) and charge extraction. However, these parameters are only applicable for solar cell structures. Meanwhile, for photoelectrocatalysis, the method suggested by Monllor-Satoca and Gomez[50] can be employed to obtain the pseudo-first-order velocity (inverse lifetime) for the charge recombination and transfer processes using a thin film electrode. However, no studies have reported the methodology using a solid electrode. This method is based on cyclic voltammetry without illumination (Fig. 5a) and the open-circuit

voltage (V_{oc}) *versus* time relaxation decay after switching off illumination. This method considers an equilibrium between the free and trapped electrons and the open-circuit voltage (OCP, V_{oc}) *versus* time relaxation decay after switching off illumination. Under these conditions, the chronoamperometry results for each photoelectrode are reported in Fig. 5c, for two conditions – A in the dark, before turning on the illumination (before illumination) and B in the dark, after turning off the illumination (after illumination). A solid electrode was used instead of a thin film electrode; Fig. 5c shows V_{oc} *versus* time. When the V_{oc} after illumination is more negative than it is in the dark, holes are preferentially transferred to solution, and the photoelectrode presents photoanodic behavior. Conversely, when V_{oc} under illumination is more positive than it is in the dark, the electrons are preferentially transferred to solution (photocathode). The first condition is adequate for the TiO_2 and $TiO_2 : N$ photoelectrodes, as confirmed in Fig. 5c. In this way, ferricyanide/ferricyanide is an adequate electrolyte to obtain the photoelectrochemical characterization of solid electrodes.

The concentration of electrons during decay ($n_{ph}(E)$) after switching off illumination can be obtained by integration of the voltammogram (Fig. 5b) between the potential steady state or stationary potential in the dark (V_{oc}) and the potential at a certain time (in this case, defined as 1.0 V *vs.* SCE) during decay as follows:[50]

$$n_{ph}(E) = \frac{1}{e_{Ad}} \int_{E_0}^{V_{oc}(t)} \frac{1}{v} dE \tag{9}$$

here, A is the geometric area of the electrode, I is the voltammogram current, v is the cyclic voltammetric scan velocity, and d is the film thickness. As a solid electrode is used in this study, d represents the thickness of the carbon paste electrode. This fit probably changes the final value of the electron concentration compared with that obtained using thin film electrodes; however, this difference will not interfere with the results because the goal is to compare the TiO_2 and $TiO_2 : N$ photoelectrodes and to investigate whether N-doping interferes with photocatalytic efficiency.[24]

The V_{oc} (open potential circuit potential) values of the TiO_2 and $TiO_2 : N$ photoelectrodes were 0.208 V and 0.439 V *vs.* SCE, respectively (Fig. 5b). The concentration of electrons during decay ($n_{ph}(E)$) was 7.108×10^{20} cm^{-3} and 6.253×10^{20} cm^{-3} for the TiO_2 and $TiO_2 : N$ photoelectrodes, respectively (Fig. 5d). As shown in Fig. 5d, the TiO_2 photoelectrode had a higher concentration of electrons than the $TiO_2 : N$ photoelectrode at different decay times. Xiang *et al.*[45] have also reported an increase in the efficiency of charge collection after doping TiO_2 with N by intensity-modulated photocurrent spectroscopy.

For photocatalysis to occur, at least two chemical processes must occur simultaneously on the catalyst: oxidation based on the transfer of the photogenerated holes and reduction involving the photogenerated electrons. Both processes are based on a precise charge balance. If the catalyst is present as particles or agglomerates, there will be interference from other processes such as the recombination of electrons and holes and/or relaxation of electrons and holes to lower energy states.
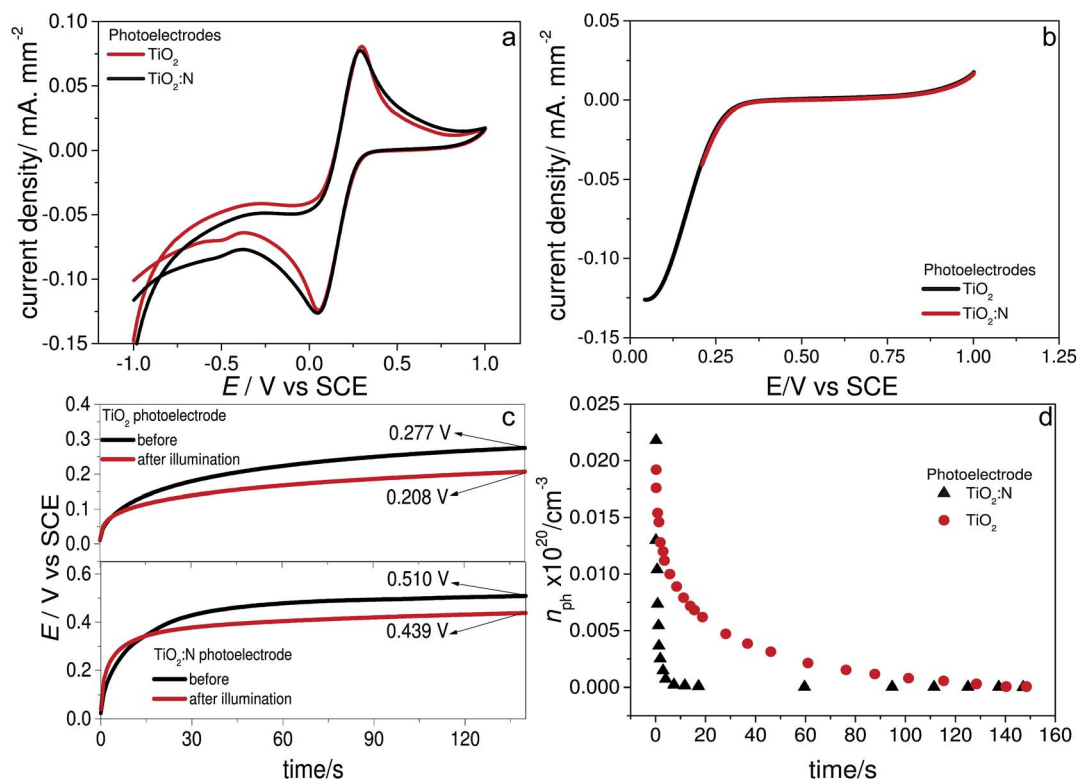
Fig. 5 (a) Cyclic voltammetry with the photoelectrodes of TiO$_2$ and TiO$_2$: N (15%), 20 mV s^{-1}, K$_3$Fe(CN)$_6$, 0.05 mol L^{-1}, without UV-C illumination, (b) insert from (a) of the region used for electron density calculations, (c) circuit open potential before and after UVC illumination for the photoelectrodes, K$_3$Fe(CN)$_6$, 0.05 mol L^{-1}, (d) relation between n_{ph} vs. time for the photoelectrodes with TiO$_2$ and TiO$_2$: N (15%).

In this regard, recombination is not desirable because it negatively affects electronic transfer, or in extreme cases, the overall processes could be inhibited. Also, in photocatalysis or photoelectrocatalysis, the visible activity of a semiconductor is important, caused by the increase in the activation of its wavelength, and consequently, recombination could occur, as the effective energy barrier is smaller. The main reason for the previously obtained result, i.e., a lower concentration of electrons in TiO$_2$: N than in TiO$_2$, is an increase in the recombination of electrons and holes or the relaxation of electrons and holes to lower energy states, as N-doping creates inter-levels in the band-gap of TiO$_2$: N. Hence, the effective energy barrier for electron concentration is smaller.

The principal question is whether the decrease in the effective energy barrier causes an inhibition of the overall process. Hence, the results obtained here are important since they demonstrate that although TiO$_2$: N may have lower energy barriers for the generation of electrons and holes, recombination may improve because of the same factor. The results of n_{ph} vs. time were similar to those observed in previous studies using thin film electrodes, confirming the perfect fit of this mathematical model with the experimental results.[50]

The relationship between the rate of transfer of electrons to acceptors, v_e, can be determined in relation to the electron concentration by:[50]

$$v_e\left(n_{ph}\right) = \frac{-1}{n_{ph}} \frac{dn_{ph}}{dt} \tag{10}$$

Fig. 6 shows the relationship between dn_{ph}/dt and n_{ph} and between k and n_{ph} for both electrodes. In the absence of effective oxidants (e$^-$ acceptors), k denotes the recombination of the accumulated electrons or intermediate molecules in photooxidation. However, in the presence of an oxidant, as in this case, the constant mainly refers to the velocity of the transfer of electrons to the acceptors.[50] Notably, a remarkable difference can be observed between the electrodes, i.e., the electron transfer in the TiO$_2$: N electrode was significantly faster than that in the TiO$_2$ electrode.

The $n_{ph}(E)$ values are similar to the densities of donors, calculated by the Nyquist plot from electrochemical impedance spectroscopy. As reported by Kang et al.,[51] the donor densities for pristine TiO$_2$ arrays are higher than those observed for TiO$_2$ arrays reduced by NaBH$_4$ (8.93 × 10^{17} and 2.06 × 10^{18} cm^{-3}, respectively).[51] They have attributed the observed increase in the donor densities to the generation of surface oxygen vacancies, which serve as electron donors, promoting a shift in the TiO$_2$ Fermi level toward the CB. Consequently, charge separation at the semiconductor electrode interface easily occurs by increasing the degree of bending of the band at the TiO$_2$ surface.[51]

In the case of the ($n_{ph}(E)$) values, surface oxygen vacancies do not increase after doping as compared to those of the undoped electrode, resulting in a shift in the TiO$_2$: N Fermi level toward the VB. This shift in the Fermi level permits the transfer of charge in the space charge region, thereby preventing efficient charge separation at the semiconductor electrode interface.
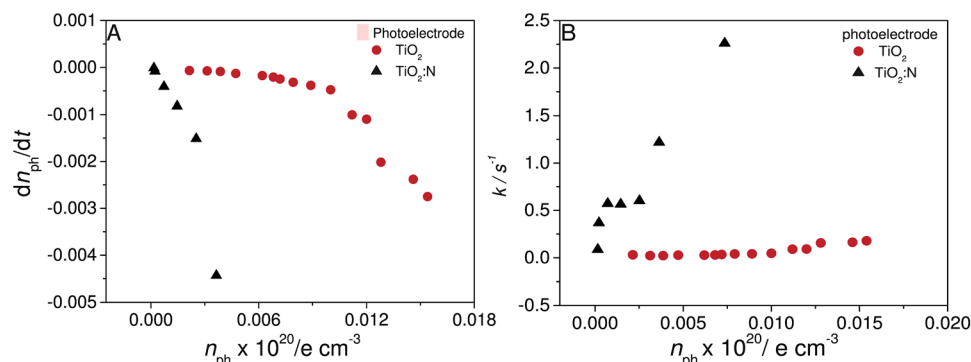
Fig. 6 Relation between dn_{ph}/dt (a) and k vs. n_{ph} (b) for the photoelectrodes with TiO₂ and TiO₂ : N.

This result confirms that doping actually creates energy inter-levels in the TiO₂ band-gap with a decrease in the effective energy barrier for electron transfer. However, these effects cause a consequent increase in the rate of electron transfer, confirming an undesirable doping effect, *i.e.*, the recombination rate of electrons increases, thereby decreasing the photocatalytic efficiency.

3.2 DFT calculations

In this section, we carry out a theoretical evaluation of the N-doping effect on the structural and electronic properties of the bulk and surface TiO₂ anatase focused on the photocatalytic behavior. Such results are useful for understanding the intrinsic effects of doping in semiconductors and infer the properties associated with bulk/surface charge migration, which is important in the overall process. Firstly, the optimized lattice parameters at the B3LYP + D level of theory ($a = 3.783$, $c = 9.570$ and $\mu = 0.208$) show excellent agreement with the experimental results.[52] For the (N^{2-})-doped model, an expansion of the unit cell that can be related to the increase in the Ti–N and Ti–O bond lengths in the axial and equatorial planes was observed, as presented in Fig. 7b. This expansion induces a large distortion in comparison to the pure TiO₆ cluster (Fig. 7a), resulting in local structural disorder associated with the electronic distribution of the paramagnetic N^{2-} species ($2s^2 2p^5$), which induces a large spin localization on the p_z orbital inducing elongation around the axial plane. On the other hand, diamagnetic doping (N^{3-}) induces a contraction of the unit cell volume, which is related to the reduced Ti–N and Ti–O bond lengths attributed to

the presence of oxygen vacancies (Fig. 7c). In this case, the structural distortion is related to the presence of a negatively charged $[TiO_6N]'$ cluster that induces the formation of oxygen vacancies $[TiO_5 \cdot V_O^{\cdot\cdot}]$, resulting in a reduced Ti^{3+} species. Since this structural disorder is associated with the titanium 3d orbitals, the corresponding electronic state must be located above the valence band maximum resulting in several changes in the electronic structure, as reported by other theoretical analyses.[34,35,53,54] Thus, the electronic structures of TiO₂ : N and TiO₂ were analyzed from density of states (DOS) and the band structure profiles presented in Fig. 8.

It was observed from the DOS results for pure TiO₂ (Fig. 8a) that the valence band (VB) is mainly composed of oxygen 2p states, whereas the conduction band (CB) is based on 3d (Ti) electronic states. Band structure profiles show an indirect band-gap between the $Y–\Gamma$ points at around 3.80 eV, in agreement with experimental reports (3.20–3.60 eV) and similar to other theoretical deviations.[55–58] The electronic results for paramagnetic (N^{2-})-doped TiO₂ (Fig. 8b) indicates a perturbation in both the VB and CB energy levels through the introduction of the nitrogen electronic states in the midgap region resulting in a narrowing band-gap of 2.44 eV. On the other hand, considering the diamagnetic (N^{3-}) scenario (Fig. 8c), it was observed that the main effects related to the doping process are associated with the creation of midgap states near to the valence band maximum (VBM), resulting in narrowing band-gap of 3.26 eV. These midgap states are mainly composed of 2p states of N and O atoms associated with 3d orbitals from the Ti^{3+} species, in excellent agreement with theoretical data reported by
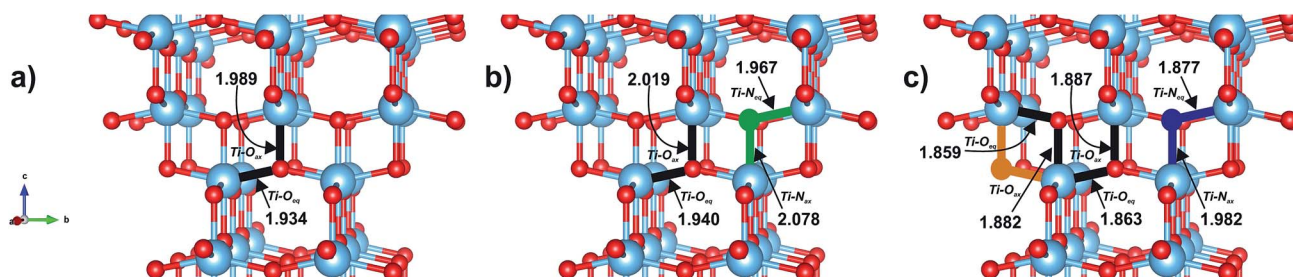

Fig. 7 Optimized local geometry and Ti−(O, N) bond distances for (a) TiO₂ (b) paramagnetic (N^{2-}) and (c) diamagnetic (N^{3-}) nitrogen doped TiO₂ anatase. Blue, red, green, purple and orange balls represent the Ti, O, N^{2-}, N^{3-} and O_{vac} species, respectively.
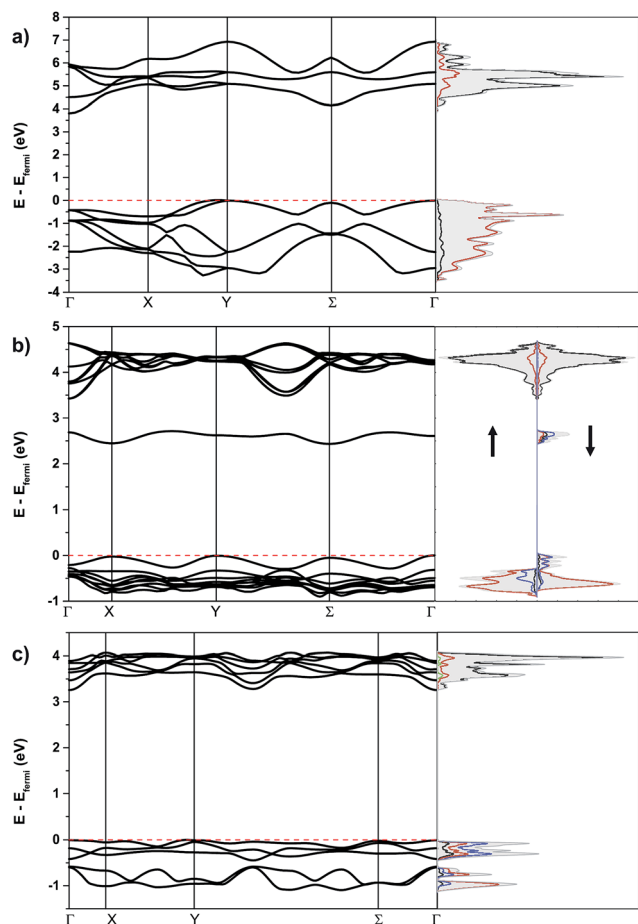
a)

b)

c)

Fig. 8 Atom-resolved density of states (DOS) and band structure profiles for the (a) pure, (b) paramagnetic (N^{2-}) and (c) diamagnetic (N^{3-}) nitrogen doped anatase TiO_2. Black, red and blue lines in the DOS correspond to the titanium, oxygen and nitrogen electronic states, respectively. The green lines in the DOS correspond to the electronic states due to vacancies. In all cases the Fermi Level was set to zero. The arrows represent up and down spin states.

Spadavecchia and co-workers.[33] Such results are in agreement with the experimental observations for the shifted VB and flat-band potential in the N-doped TiO_2 samples (Fig. 3) suggesting improved sunlight-driven photocatalytic behavior. In addition to the band-gap reduction, to favor the creation of electron–hole pairs, the recombination process plays a fundamental role in the photocatalytic activity. The photocatalytic behavior of anatase TiO_2 is strictly related to the indirect nature of the band-gap excitation due to the higher charge carrier lifetime compared with that of direct band-gap semiconductors.[59] However, the band structure profiles for both the paramagnetic (N^{2-}) and diamagnetic (N^{3-}) doped TiO_2 scenarios (Fig. 8b and c) indicate that both the VBM and CBM were shifted from their Y and Γ points, respectively. In the first case, the creation of midgap states associated with the paramagnetic N^{2-} species modifies the band distribution resulting in a quite small energy difference between the direct (2.46 eV X–X; 2.48 eV Σ–Σ) and indirect (2.44 eV Y–X; 2.43 eV Y–Σ) band-gap values (Fig. 8b). Otherwise, for diamagnetic doping (N^{3-}) the CBM remains

similar to that of the pure TiO_2, while the VBM is shifted from the Y point behaving as a flat band, where the energy differs between the direct (3.26 eV Γ–Γ) and indirect (3.27 eV Y–Γ; 3.28 eV Σ–Γ) band-gap values (Fig. 8c). Therefore, the electronic structures of both nitrogen doped TiO_2 scenarios are more susceptible to electron–hole recombination than pure TiO_2 (Fig. 8a) due to having the smallest direct band-gap. These data support the experimental observation presented in Fig. 6, which suggests a higher electron-recombination rate for the N-doped samples in comparison to the pure anatase. Furthermore, despite the difference between the mechanism associated with the doping of both paramagnetic and diamagnetic nitrogen atoms, theoretical results indicate that both species act in the band-gap region, which becomes narrowed and direct, resulting in an extended electron–hole pair recombination.

In order to compare the N-doping process on the bulk and surface-oriented TiO_2 nanoparticles, periodic slab models were simulated at the DFT/B3LYP + D level of theory considering a 001-oriented supercell with an 18-layer slab thickness (36 atoms). The calculated surface energy for the pure anatase (001) surface (1.56 J m^{-2}) exhibits good agreement with other theoretical reports.[60,61] In this case, only the paramagnetic (N^{2-}) scenario was considered due to the huge computational cost of diamagnetic doping, which consists of substitutional N^{3-} species summed to the number of oxygen vacancies. Further studies considering this scenario are in progress. However, paramagnetic and diamagnetic nitrogen doping in bulk anatase TiO_2 induces a similar effect on the electronic structure considering the photocatalytic efficiency, as discussed above, indicating that N^{2-} doped 001-oriented TiO_2 nanoparticles are useful for predicting the main effect behind the photocatalytic behavior.

Electronic density of state and band structure profiles for the pure and N-doped anatase (001) surfaces are presented in Fig. 9. The electronic occupations at the valence and conduction bands for the 001-oriented anatase (Fig. 9a) shows the same pattern of distribution observed in the bulk (Fig. 8a) with an indirect band-gap around 2.96 eV between the M–Γ points. Regarding the N-doping process (Fig. 9b), DOS results reveal the creation of midgap states, mainly on the top of the valence band, composed of nitrogen (2p) states. It is important to note that the doping mechanisms at the bulk/surface exhibit different electronic structures because nitrogen replacement on the two-coordinated outermost oxygen surface keeps the dangling bonds at an anionic site resulting in a higher amount of spin-density (0.996 a.u.) in comparison to the three-fold coordinated site in the bulk (0.885 a.u.). Such an effect induces a smallest band-gap of around 1.84 eV; however, the nature of the electronic transition was modified to a direct excitation between N–N points suggesting a higher electron recombination rate in comparison to the pure 001-oriented TiO_2. Therefore, despite the band-gap reduction, the bulk and surface nitrogen doping mechanism also induces a large electron–hole recombination rate reducing the photocatalytic efficiency.

Besides the band-gap nature, photocatalytic efficiency is also affected by the mobility of photoinduced electrons and holes. In
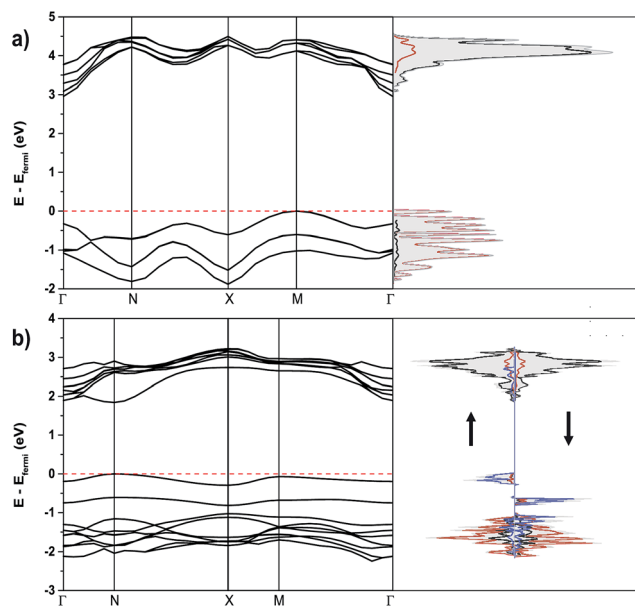
Fig. 9 Atom-resolved density of state and band structure profiles for the (a) pure and (b) (N^{2-})-doped 001-surface oriented TiO_2 anatase. Black, red and blue lines in the DOS correspond to the titanium, oxygen and nitrogen electronic states, respectively. For the band structures, the Fermi level was set to zero. The arrows represent up and down spin states.

this context, the effective mass of electrons and holes plays a fundamental role in the diffusion (D) of free charge carriers, as follows:

$$D = \frac{k_B T}{e} \qquad (11)$$

$$\mu = e\frac{\tau}{m^*} \qquad (12)$$

where μ corresponds to the mobility, which is linked to effective mass (m^*) and the collision time (τ) of the charge carrier. Therefore, D increases if the effective mass of the photo-generated carriers becomes lighter, reflective of enhanced photocatalytic efficiency. Furthermore, the ratio between the effective mass of electrons (m_e^*) and holes (m_h^*) is a powerful tool to predict the electron/hole pair stability with respect to the recombination process. In this case, a larger effective mass

difference induces distinct mobilities, which reduce the electron–hole pair recombination increasing the photocatalytic efficiency.[62–64]

In order to explain the photocatalytic performance of both the pure and N-doped TiO_2 anatase, the effective masses of electrons (m_e^*) and holes (m_h^*) were calculated (Table 1) by fitting parabolic functions considering a small region near the CBM and VBM.[62–64]

Theoretical results for pure TiO_2 show that the effective mass of holes (m_h^*) is sensitive to crystal growth, in agreement with the different bands' dispersion near the CBM for the bulk and 001-surface models (Fig. 8a and 9a). In this case, the electron mobility is higher in the bulk, indicating that photoinduced charge carriers can easily migrate to the surface to participate in the photocatalytic process. Furthermore, the higher m_e^*/m_h^* suggests that, once localized on the surface, the electron mobility is reduced while the hole remains stable, which is beneficial for reducing the recombination process.

Regarding the paramagnetic nitrogen (N^{2-}) doping process into anatase TiO_2, similar behavior was observed for the bulk and surface models. In both cases, theoretical results indicate that the electron and hole effective masses increase with doping, reducing the m_e^*/m_h^* which is reflective of a higher electron–hole pair recombination rate in accordance with experimental results. The main differences between the results were assigned to the nitrogen effect at the effective mass of holes in both models, which can be associated with the bands' dispersion related to the two-fold and three-fold coordinated N^{2-} species. Further, considering the N^{3-} scenario, it can be seen that diamagnetic nitrogen doping also significantly reduces the m_e^*/m_h^* ratio, increasing the electron–hole pair recombination, which can be associated with the creation of vacancies, resulting in a Ti^{3+} species that acts as an electron-trap. Therefore, in all cases, the nitrogen doping process reduces the m_e^*/m_h^* ratio making it difficult for the separation of photogenerated electrons from their associated holes, increasing the probability of their recombination. Despite the differences from the experimental measurements (caused by limitations of calculations in environments other than a vacuum), these results confirm the analysis of photoelectrochemical measurements, where a similar tendency is shown, supporting our hypothesis.

Table 1 Effective mass of electrons (m_e^*) and holes (m_h^*) for the pure and N-doped TiO_2 anatase at the CBM and VBM along a specific direction in reciprocal space. TiO_2 : (N^{2-}) and TiO_2 : (N^{3-}) correspond to the paramagnetic and diamagnetic nitrogen doped models, while m_o is the standard electron rest mass

Models			Direction	m_e^*/m_o	m_h^*/m_o
Bulk	TiO_2		Y–Γ	0.46	0.14
	TiO_2 : (N^{2-})		X–X	0.56	0.44
			Y–Σ	0.53	0.49
	TiO_2 : (N^{3-})		Γ–Γ	0.25	0.17
			Y–Γ	0.21	0.17
Surface	TiO_2		M–Γ	0.84	0.13
	TiO_2 : (N^{2-})		N–N	0.80	0.23

4 Conclusions

This study reports the electronic structure and the effect of $TiO_2 : N$ nanoparticles on a photoactivated process. This investigation, based on experimental and theoretical results, confirmed the creation of inter-levels by N-doping. The replacement of an oxygen atom by nitrogen in the anatase structure modified the energy levels, which reduces the band-gap by 1 eV due to a shift in upper energy level. In addition, theoretical analysis showed a possible direct band-gap in both the paramagnetic and diamagnetic $TiO_2 : N$ models, which would imply an increase in the generation of charges, albeit with faster recombination. This combined approach was notably useful for interpreting the electron–hole recombination process on photocatalytic activity using $TiO_2 : N$. Therefore, N-doped TiO_2 anatase is a self-consistent system because it supports the photocatalysis process through a highly decreased band-gap; however, it increases electron–hole pair recombination from the m_e^*/m_h^* ratio under UVC illumination.

Acknowledgements

References

1 A. Ginebreda, M. Kuzmanovic, H. Guasch, M. L. de Alda, J. C. Lopez-Doval, I. Munoz, M. Ricart, A. M. Romani, S. Sabater and D. Barcelo, *Sci. Total Environ.*, 2014, **468**, 715–723.

2 F. Ricciardi, C. Bonnineau, L. Faggiano, A. Geiszinger, H. Guasch, J. Lopez-Doval, J. Munoz, L. Proia, M. Ricart, A. Romani and S. Sabater, *TrAC, Trends Anal. Chem.*, 2009, **28**, 592–602.

3 P. M. Peltzer, R. C. Lajmanovich, A. M. Attademo, C. M. Junges, M. C. Cabagna-Zenklusen, M. R. Repetti, M. E. Sigrist and H. Beldomenico, *Ecotoxicol. Environ. Saf.*, 2013, **98**, 142–151.

4 T. Woignier, P. Fernandes, A. Soler, F. Clostre, C. Carles, L. Rangon and M. Lesueur-Jannoyer, *J. Hazard. Mater.*, 2013, **262**, 357–364.

5 Y. Horiuchi, T. Toyao, M. Takeuchi, M. Matsuoka and M. Anpo, *Phys. Chem. Chem. Phys.*, 2013, **15**, 13243–13253.

6 A. Primo, A. Corma and H. Garcia, *Phys. Chem. Chem. Phys.*, 2011, **13**, 886–910.

7 I. Oller, S. Malato, J. A. Sanchez-Perez, M. I. Maldonado and R. Gasso, *Catal. Today*, 2007, **129**, 69–78.

8 M. N. Siddiqui and M. A. Gondal, *J. Environ. Sci. Health, Part A: Environ. Sci. Eng. Toxic Hazard. Subst. Control*, 2014, **49**, 52–58.

9 F. Chowdhury, K. S. Begum, S. M. F. Hasan and M. S. Alam, *Optoelectron. Adv. Mater., Rapid Commun.*, 2011, **5**, 356–359.

10 S. Kuk, S. Bang, I. Kim, S. Jeon, H. Jeon, H. H. Park and H. J. Chang, *Eco-Materials Processing and Design VIII*, 2007, vol. 544–545, pp. 689–692.

11 J. K. Burdett, T. Hughbanks, G. J. Miller, J. W. Richardson Jr and J. V. Smith, *J. Am. Chem. Soc.*, 1987, **109**, 3639–3646.

12 J. Pan and S. P. Jiang, *J. Colloid Interface Sci.*, 2016, **469**, 25–30.

13 Y. Zheng, J. H. Cai, K. L. Lv, J. Sun, H. P. Ye and M. Li, *Appl. Catal., B*, 2014, **147**, 789–795.

14 M. C. Tsai, J. Y. Lee, P. C. Chen, Y. W. Chang, Y. C. Chang, M. H. Yang, H. T. Chiu, I. N. Lin, R. K. Lee and C. Y. Lee, *Appl. Catal., B*, 2014, **147**, 499–507.

15 G. B. Soares, B. Bravin, C. M. P. Vaz and C. Ribeiro, *Appl. Catal., B*, 2011, **106**, 287–294.

16 X. K. Wang, C. Wang, W. Q. Jiang, W. L. Guo and J. G. Wang, *Chem. Eng. J.*, 2012, **189**, 288–294.

17 Y. X. Zhao, X. F. Qiu and C. Burda, *Chem. Mater.*, 2008, **20**, 2629–2636.

18 X. X. Lin, F. Rong, D. G. Fu and C. W. Yuan, *Powder Technol.*, 2012, **219**, 173–178.

19 N. S. Allen, M. Edge, J. Verran, L. Caballero, C. Abrusci, J. Stratton, J. Maltby and C. Bygott, *Open Mater. Sci. J.*, 2009, **3**, 6–27.

20 A. V. Vinogradov, V. V. Vinogradov and A. V. Agafonov, *J. Alloys Compd.*, 2013, **581**, 675–678.

21 L. Jiang, T. You and W. Q. Deng, *Nanotechnology*, 2013, **24**, 415401.

22 A. I. Kokorin, E. A. Konstantinova and H. Kisch, *Kinet. Catal.*, 2013, **54**, 373–377.

23 M. Dawson, G. B. Soares and C. Ribeiro, *J. Solid State Chem.*, 2014, **215**, 211–218.

24 T. Berger, D. Monllor-Satoca, M. Jankulovska, T. Lana-Villarreal and R. Gomez, *ChemPhysChem*, 2012, **13**, 2824–2875.

25 R. Beranek, B. Neumann, S. Sakthivel, M. Janczarek, T. Dittrich, H. Tributsch and H. Kisch, *Chem. Phys.*, 2007, **339**, 11–19.

26 G. B. Soares, C. M. P. Vaz, C. Ribeiro and I. Hermans, *Electrocatalysis*, 2015, **6**, 92–101.

27 A. D. Becke, *J. Chem. Phys.*, 1993, **98**, 5648–5652.

28 C. T. Lee, W. T. Yang and R. G. Parr, *Phys. Rev. B: Condens. Matter Mater. Phys.*, 1988, **37**, 785–789.

29 S. Grimme, *J. Chem. Phys.*, 2006, **124**, 034108.

30 R. Dovesi, R. Orlando, B. Civalleri, C. Roetti, V. R. Saunders and C. M. Zicovich-Wilson, *Z. Kristallogr.*, 2005, **220**, 571–573.

31 Y. Ortega, O. Lamiel-Garcia, D. F. Hevia, S. Tosoni, J. Oviedo, M. A. San-Miguel and F. Illas, *Surf. Sci.*, 2013, **618**, 154–158.

32 A. R. Albuquerque, A. Bruix, J. R. Sambrano and F. Illas, *J. Phys. Chem. C*, 2015, **119**, 4805–4816.

33 F. Spadavecchia, G. Cappelletti, S. Ardizzone, M. Ceotto and L. Falciola, *J. Phys. Chem. C*, 2011, **115**, 6381–6391.

34 C. Di Valentin, E. Finazzi, G. Pacchioni, A. Selloni, S. Livraghi, M. C. Paganini and E. Giamello, *Chem. Phys.*, 2007, **339**, 44–56.

35 C. Di Valentin, G. Pacchioni and A. Selloni, *Phys. Rev. B: Condens. Matter Mater. Phys.*, 2004, **70**, 085116.

36 H. J. Monkhorst and J. D. Pack, *Phys. Rev. B: Condens. Matter Mater. Phys.*, 1976, **13**, 5188–5192.

37 R. Dovesi, V. R. Saunders, C. Roetti, R. Orlando, C. M. Zicovich-Wilson, F. Pascale, B. Civalleri, K. Doll, N. M. Harrison, I. J. Bush, P. D'Arco and M. Llunell, *CRYSTAL09 User's Manual*, 2009.

38 G. Sophia, P. Baranek, C. Sarrazin, M. Rerat and R. Dovesi, *Phase Transitions*, 2013, **86**, 1069–1084.

39 C. Gatti, V. R. Saunders and C. Roetti, *J. Chem. Phys.*, 1994, **101**, 10686–10696.

40 A. Ambrosi and M. Pumera, *Chem.–Eur. J.*, 2016, **22**, 153–159.

41 C. Brett and A. Brett, *Electrochemistry: Principles, Methods, and Applications*, Oxford University Press, 1993, p. 427.

42 D. Martin-Yerga, E. C. Rama and A. Costa-Garcia, *J. Electrochem. Soc.*, 2016, **163**, B176–B179.

43 R. Beranek, *Adv. Phys. Chem.*, 2011, **2011**, 786759.

44 N. Sato, *Semiconductor photoelectrodes*, Elsevier Science, 1998.

45 P. Xiang, X. Li, H. Wang, G. Liu, T. Shu, Z. Zhou, Z. Ku, Y. Rong, M. Xu, L. Liu, M. Hu, Y. Yang, W. Chen, T. Liu, M. Zhang and H. Han, *Nanoscale Res. Lett.*, 2011, **6**, 606.

46 J. Q. Li, L. P. Li, L. Zheng, Y. Z. Xian and L. T. Jin, *Electrochim. Acta*, 2006, **51**, 4942–4949.

47 M. V. B. Zanoni, J. J. Sene and M. A. Anderson, *J. Photochem. Photobiol., A*, 2003, **157**, 55–63.

48 M.-L. Guo, X.-D. Zhang, C.-T. Liang and G.-Z. Jia, *Chin. Phys. Lett.*, 2010, **27**, 057103.

49 X. Li, D.-T. Wang, J.-F. Chen and X. Tao, *Electrochim. Acta*, 2012, **80**, 126–132.

50 D. Monllor-Satoca and R. Gomez, *J. Phys. Chem. C*, 2008, **112**, 139–147.

51 Q. Kang, J. Cao, Y. Zhang, L. Liu, H. Xu and J. Ye, *J. Mater. Chem. A*, 2013, **1**, 5766–5774.

52 C. J. Howard, T. M. Sabine and F. Dickson, *Acta Crystallogr., Sect. B: Struct. Sci.*, 1991, **47**, 462–468.

53 A. K. Rumaiz, J. C. Woicik, E. Cockayne, H. Y. Lin, G. H. Jaffari and S. I. Shah, *Appl. Phys. Lett.*, 2009, **95**, 262111.

54 S. Livraghi, M. C. Paganini, E. Giamello, A. Selloni, C. Di Valentin and G. Pacchioni, *J. Am. Chem. Soc.*, 2006, **128**, 15666–15671.

55 L. Miao, S. Tanemura, P. Jin, K. Kaneko, A. Terai and N. Nabatova-Gabain, *J. Cryst. Growth*, 2003, **254**, 100–106.

56 H. Tang, F. Levy, H. Berger and P. E. Schmid, *Phys. Rev. B: Condens. Matter Mater. Phys.*, 1995, **52**, 7771–7774.

57 R. Sanjinés, H. Tang, H. Berger, F. Gozzo, G. Margaritondo and F. Lévy, *J. Appl. Phys.*, 1994, **75**, 2945–2951.

58 A. R. Albuquerque, M. L. Garzim, I. M. G. dos Santos, V. Longo, E. Longo and J. R. Sambrano, *J. Phys. Chem. A*, 2012, **116**, 11731–11735.

59 T. Luttrell, S. Halpegamage, J. Tao, A. Kramer, E. Sutter and M. Batzill, *Sci. Rep.*, 2014, **4**, 4043.

60 A. Beltran, J. R. Sambrano, M. Calatayud, F. R. Sensato and J. Andres, *Surf. Sci.*, 2001, **490**, 116–124.

61 A. R. Albuquerque, I. M. G. Santos and J. R. Sambrano, *Quim. Nova*, 2014, **37**, 1318–1323.

62 J. Zhang, P. Zhou, J. Liu and J. Yu, *Phys. Chem. Chem. Phys.*, 2014, **16**, 20382–20386.

63 T. Le Bahers, M. Rerat and P. Sautet, *J. Phys. Chem. C*, 2014, **118**, 5997–6008.

64 P. Liao and E. A. Carter, *Chem. Soc. Rev.*, 2013, **42**, 2401–2422.